Article

Attosecond pulse shaping using a seeded free-electron laser

https://doi.org/10.1038/s41586-020-2005-6

Received: 24 May 2019

Accepted: 5 November 2019

Published online: 10 February 2020

Check for updates

Praveen Kumar Maroju[1], Cesare Grazioli[2], Michele Di Fraia[3], Matteo Moioli[1], Dominik Ertel[1], Hamed Ahmadi[1], Oksana Plekan[3], Paola Finetti[3], Enrico Allaria[3], Luca Giannessi[3,4], Giovanni De Ninno[3,5], Carlo Spezzani[3], Giuseppe Penco[3], Simone Spampinati[3], Alexander Demidovich[3], Miltcho B. Danailov[3], Roberto Borghes[3], George Kourousias[3], Carlos Eduardo Sanches Dos Reis[3], Fulvio Billé[3], Alberto A. Lutman[6], Richard J. Squibb[7], Raimund Feifel[7], Paolo Carpeggiani[8], Maurizio Reduzzi[9], Tommaso Mazza[10], Michael Meyer[10], Samuel Bengtsson[11], Neven Ibrakovic[11], Emma Rose Simpson[11], Johan Mauritsson[11], Tamás Csizmadia[12], Mathieu Dumergue[12], Sergei Kühn[12], Harshitha Nandiga Gopalakrishna[12], Daehyun You[13], Kiyoshi Ueda[13], Marie Labeye[14], Jens Egebjerg Bækhøj[14], Kenneth J. Schafer[14], Elena V. Gryzlova[15], Alexei N. Grum-Grzhimailo[15], Kevin C. Prince[3], Carlo Callegari[3] & Giuseppe Sansone[1]✉

Attosecond pulses are central to the investigation of valence- and core-electron dynamics on their natural timescales[1–3]. The reproducible generation and characterization of attosecond waveforms has been demonstrated so far only through the process of high-order harmonic generation[4–7]. Several methods for shaping attosecond waveforms have been proposed, including the use of metallic filters[8,9], multilayer mirrors[10] and manipulation of the driving field[11]. However, none of these approaches allows the flexible manipulation of the temporal characteristics of the attosecond waveforms, and they suffer from the low conversion efficiency of the high-order harmonic generation process. Free-electron lasers, by contrast, deliver femtosecond, extreme-ultraviolet and X-ray pulses with energies ranging from tens of microjoules to a few millijoules[12,13]. Recent experiments have shown that they can generate subfemtosecond spikes, but with temporal characteristics that change shot-to-shot[14–16]. Here we report reproducible generation of high-energy (microjoule level) attosecond waveforms using a seeded free-electron laser[17]. We demonstrate amplitude and phase manipulation of the harmonic components of an attosecond pulse train in combination with an approach for its temporal reconstruction. The results presented here open the way to performing attosecond time-resolved experiments with free-electron lasers.

The intensities and relative phases between the harmonics $q\omega_F$ (with q an integer and ω_F the fundamental frequency) in an extreme ultraviolet (XUV) frequency comb determine the temporal structure of the resulting attosecond pulse train. The intensities of the harmonics can be easily measured using a (photon or electron) spectrometer. Phase information, which is harder to come by, is usually obtained by observing the interference between different pathways leading to states with the same final energy, where the phase to be characterized is included in at least one of the pathways. With XUV pulses, the natural observable is a photoelectron, hence different pathways into the ionization continuum are studied. The XUV frequency comb produced by high-order harmonic generation (HHG) consists of odd-integer harmonics of the fundamental field, and the ionization process takes place in the presence of a near-infrared (NIR) dressing field with the same frequency ω_F. Under these conditions, additional photons may be absorbed or emitted, producing a single sideband halfway between the main photoelectron peaks. Each sideband can be populated through two pathways leading to final states of the same parity and this results in a variation in sideband amplitude as a function of the relative phase of the two pathways. If the XUV and fundamental fields are precisely synchronized, as they can be in HHG, then delaying the fields with respect to each other reveals the phase information[4,18].

In our study, the harmonic comb was generated by the seeded free-electron laser (FEL) FERMI, which uses an ultraviolet pulse ($\omega_{UV} = \omega_F = 4.69$ eV) derived from a frequency-tripled NIR pulse ($\omega_{NIR} = \omega_{UV}/3$) as the seed. Three ($q = 7, 8, 9$) and four ($q = 7, 8, 9, 10$)

[1]Physikalisches Institut, Albert-Ludwigs-Universität, Freiburg, Germany. [2]ISM-CNR, Trieste LD2 Unit, Trieste, Italy. [3]Elettra-Sincrotrone Trieste SCpA, Basovizza, Trieste, Italy. [4]Istituto Nazionale di Fisica Nucleare, Laboratori Nazionali di Frascati, Rome, Italy. [5]Laboratory of Quantum Optics, University of Nova Gorica, Nova Gorica, Slovenia. [6]SLAC National Accelerator Laboratory, Menlo Park, CA, USA. [7]Department of Physics, University of Gothenburg, Gothenburg, Sweden. [8]Institut für Photonik, Technische Universität Wien, Vienna, Austria. [9]Dipartimento di Fisica, Politecnico di Milano, Milan, Italy. [10]European XFEL GmbH, Schenefeld, Germany. [11]Department of Physics, Lund University, Lund, Sweden. [12]ELI-ALPS, ELI-Hu Kft, Szeged, Hungary. [13]Institute of Multidisciplinary Research for Advanced Materials, Tohoku University, Sendai, Japan. [14]Department of Physics and Astronomy, Louisiana State University, Baton Rouge, LA, USA. [15]Skobeltsyn Institute of Nuclear Physics, Lomonosov Moscow State University, Moscow, Russia. ✉e-mail: giuseppe.sansone@physik.uni-freiburg.de

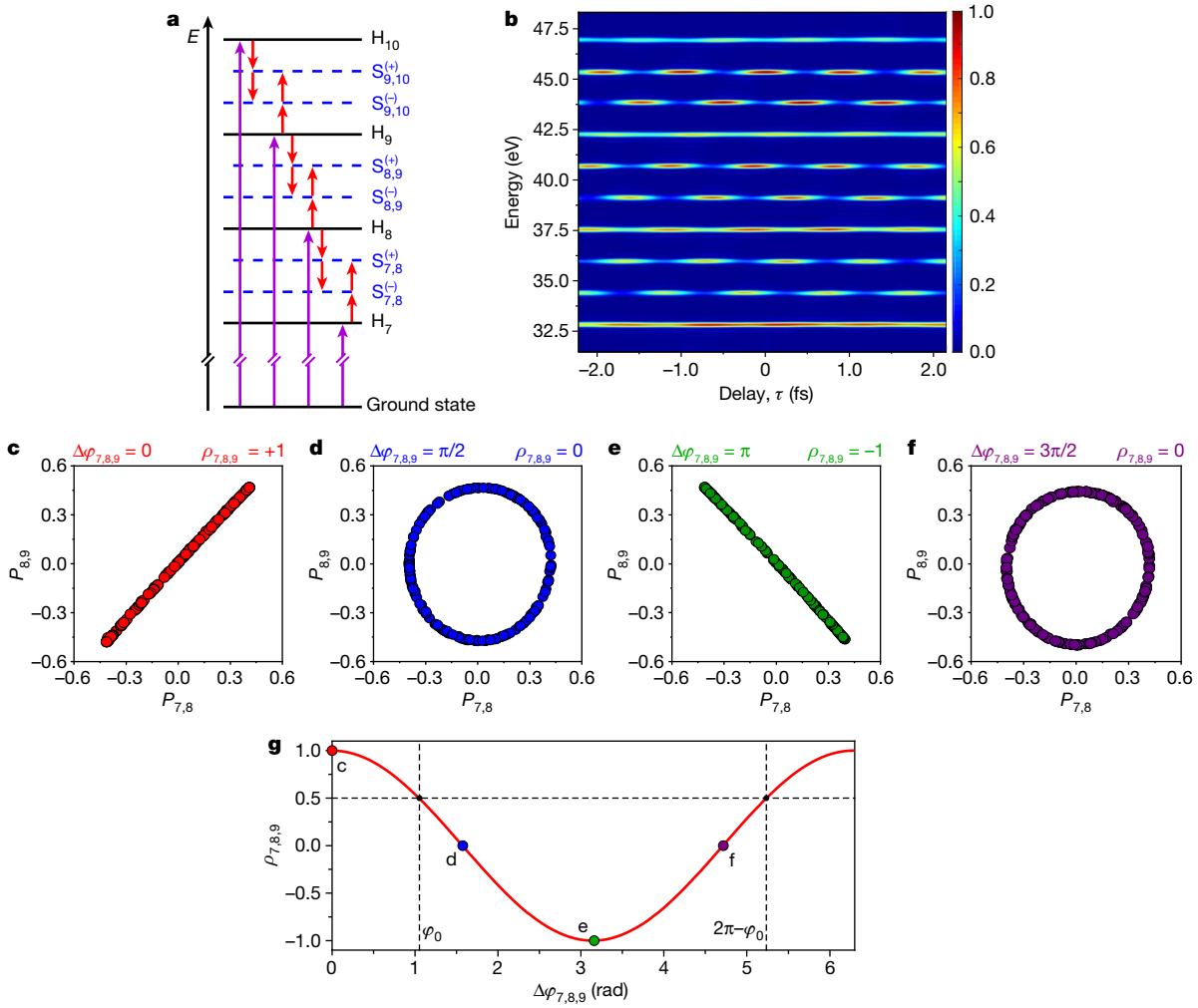

Fig. 1 | Multi-photon sideband generation and principle of the measurement. a, Schematic view of multi-NIR-photon sideband generation. Shown are the energy levels of the photoelectrons generated by the harmonics of the FEL (H_7–H_{10}; magenta arrows) and by the additional absorption and emission of one and two NIR photons ($S^{(\pm)}_{q,q+1}$; red arrows). **b**, Expected normalized intensity of the photoelectron spectra as a function of the relative delay τ between the train of attosecond pulses and the NIR field along the (positive) common direction of polarization of the two fields. The photoelectron spectra are characterized by an oscillation with a period $T = 2\pi/(3\omega_{NIR})$. **c**–**f**, Correlation plots of the oscillating components of the sidebands ($P_{7,8}$, $P_{8,9}$) for four phase differences $\Delta\varphi_{7,8,9}$; 0 (**c**), π/2 (**d**), π (**e**) and 3π/2 (**f**). At the top of each plot is shown the value of $\Delta\varphi_{7,8,9}$ (left) and $\rho_{7,8,9}$ (right). **g**, Evolution of the correlation coefficient $\rho_{7,8,9}$ as a function of $\Delta\varphi_{7,8,9}$, showing the locations corresponding to the plots **c**–**f**. The intensity of the NIR pulse is $I_{NIR} = 1.5 \times 10^{11}$ W cm^{-2}.

harmonics of ω_{UV} were generated using two different undulator configurations (see Extended Data Fig. 1 and Extended Data Table 1). To characterize the pulses, photoionization took place in the presence of a field with frequency ω_{NIR} leading to the formation of two sidebands between each pair of the main XUV peaks (see Fig. 1a). The two sidebands $S^{(\pm)}_{q,q+1}$ can be each populated through two paths characterized by a different number of exchanged NIR photons: the absorption of one photon of the harmonic q and one (two) NIR photon, or the absorption of one photon of the harmonic $q+1$ and the emission of two (one) NIR photons. The difference in parity of the final states of the interfering pathways determines an asymmetry in the photoionization emission. If the observation is restricted along a single direction, the intensity of the sidebands oscillates as a function of the delay τ between the NIR and XUV pulse (see Fig. 1b)

$$S^{(\pm)}_{q,q+1}(\tau) \propto 1 + \alpha_{q,q+1} \cos\left[\varphi_{q+1} - \varphi_q + 3\omega_{NIR}\tau\right] = 1 \pm P_{q,q+1}(\tau) \qquad (1)$$

where $\alpha_{q,q+1}$ depends on the intensity and energy of the two harmonics q and $q+1$ with phases φ_q and φ_{q+1}, on the photoelectron energy, and on the intensity of the NIR pulse, and the equality defines the oscillating component of the sideband intensity $P_{q,q+1}$ under the approximations detailed in the Supplementary Information. If the delay τ could be precisely controlled, then the relative phase between consecutive harmonics could be estimated from the time shift between the oscillations of the sidebands.

This approach cannot be applied directly to the reconstruction of the relative phase of multiple harmonics generated by an FEL owing to the lack of subcycle synchronization between the harmonics and the NIR field[19], which completely washes out the delay dependence of the sideband oscillations. The information can be still retrieved, however, through a correlation analysis of the fluctuating sideband intensities measured on a single-shot basis. This approach is presented in Fig. 1c–f, which shows the simulated correlation plots of the oscillating components $P_{8,9}$ and $P_{7,8}$ of the sidebands for a random variation of the delay τ in the range ±3 fs, which is the typical delay jitter measured in the experiment[20]. The correlation plot eliminates the explicit dependence on τ and results in an ellipse, the shape of which depends on the phase difference:

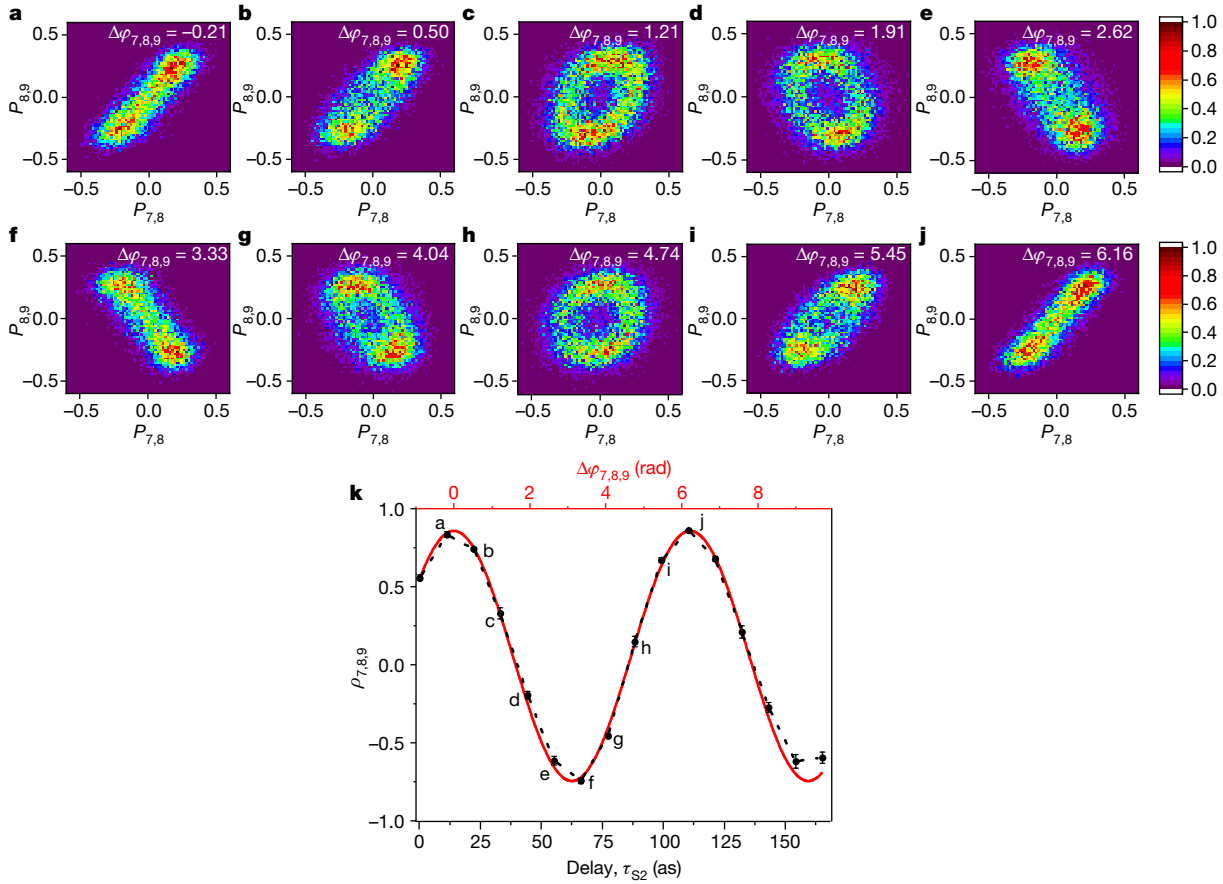

Fig. 2 | Correlation plots of the oscillating components of the sidebands and retrieval of phase difference $\Delta\varphi_{7,8,9}$. a–**j**, Evolution of the correlation plots of the oscillating components of the sidebands ($P_{7,8}$, $P_{8,9}$) for increasing values of the delay τ_{s2} introduced by the phase shifter PS_2 (Extended Data Fig. 1a). At the top right of each panel is given the value of $\Delta\varphi_{7,8,9}$. The colour scale indicates the density of single-shot experimental points normalized to unity for each panel. **k**, Evolution of the correlation coefficient $\rho_{7,8,9}$ as a function of the delay τ_{s2} (black points and dashed line) and the sinusoidal fit (red). The $\Delta\varphi_{7,8,9}$ upper x axis (red) was obtained by assigning the maxima of the fit to the values $\Delta\varphi_{7,8,9} = 2m\pi$, where m is an integer. Letters a–j show the locations corresponding to the data shown in the panels above. The error bars are the standard deviation of the average correlation coefficient $\rho_{7,8,9}$ evaluated over ten sets of experimental data (each set consists of 1,200 single-shot points). The intensity of the NIR pulse was estimated to be $I_{NIR} \approx 1.5 \times 10^{12}$ W cm^{-2}. The value of the correlation parameters, the phase differences and the corresponding errors are presented in Extended Data Table 2.

$$\Delta\varphi_{q-1,q,q+1} = \varphi_{q+1} + \varphi_{q-1} - 2\varphi_q \quad (2)$$

The intensity profile of the pulse train depends only on this phase difference (apart from a trivial time shift; see Supplementary Information). Depending on the phase difference $\Delta\varphi_{7,8,9}$, the plot evolves from a linear distribution with positive correlation (Fig. 1c), to a circle (Fig. 1d), to a linear distribution with negative correlation (Fig. 1e), and finally back to a circle (Fig. 1f). These changes clearly indicate that the shape of the correlated distribution is related to the synchronization of the three harmonics (the complete evolution as a function of the phase difference is presented in Extended Data Fig. 2). The phase information can be derived from the distribution by evaluating its correlation coefficient $\rho_{q-1,q,q+1}$ (see Supplementary Information), which quantifies the extent to which the two oscillating components oscillate perfectly in phase ($\Delta\varphi_{q-1,q,q+1} = 0$ and $\rho_{q-1,q,q+1} = +1$) or out of phase ($\Delta\varphi_{q-1,q,q+1} = \pi$ and $\rho_{q-1,q,q+1} = -1$). The correlation coefficient oscillates as a function of the phase difference $\Delta\varphi_{7,8,9}$ as shown Fig. 1g, and it closely resembles a cosine function. Two different values of $\Delta\varphi_{7,8,9}$ correspond to the same value of the correlation coefficient: φ_0 and $2\pi - \varphi_0$. This ambiguity can be resolved in the experiment by controlling the modulus and sign of the phase differences between the harmonics (see Supplementary Information). Simulations based on the solution of the time-dependent Schrödinger equation confirmed the validity of our approach (see Extended Data Fig. 3).

In the experiment, the intensity of the harmonics was independently controlled by tuning the undulator gaps and the dispersive section of the electron transport optics. The phase between the harmonics was controlled by phase shifters[21,22], which introduce a delay τ_{si} (i indicates the ith-phase shifter) for a selected harmonic q, affecting the phase difference $\Delta\varphi_{q-1,q,q+1}$, through a term $q\omega_{UV}\tau_{si}$ (see Extended Data Fig. 1). In this respect, seeded FELs offer a superior degree of control with respect to HHG sources, for which the intensities and phases of the single harmonic cannot be independently controlled.

Figure 2a–j presents the experimental results for the three-harmonic case, for different delays τ_{s2} introduced on the ninth harmonic. These measurements indicate a periodic evolution of the correlated distributions in close agreement with the theoretical prediction. A partial broadening of the distributions is attributed to the shot-to-shot fluctuations of the single harmonic intensity. The correlation coefficients $\rho_{7,8,9}$ (black points and dotted line in Fig. 2k) and the fit (red curve) clearly follow a cosine evolution in good agreement with the simulations. The maxima of the fit were assigned to the phase differences $\Delta\varphi_{7,8,9} = 0, 2\pi$ (see upper x axis in Fig. 2k) and the curve was used to assign a phase difference $\Delta\varphi_{7,8,9}$ to each delay τ_{s2}. The error in the estimation of the phase difference depends on the slope of the curve (which depends on the NIR intensity) and was typically in the range 0.05–0.1 rad for our experimental conditions (see Supplementary Information). The characterization of pulses with reproducible temporal structure gives

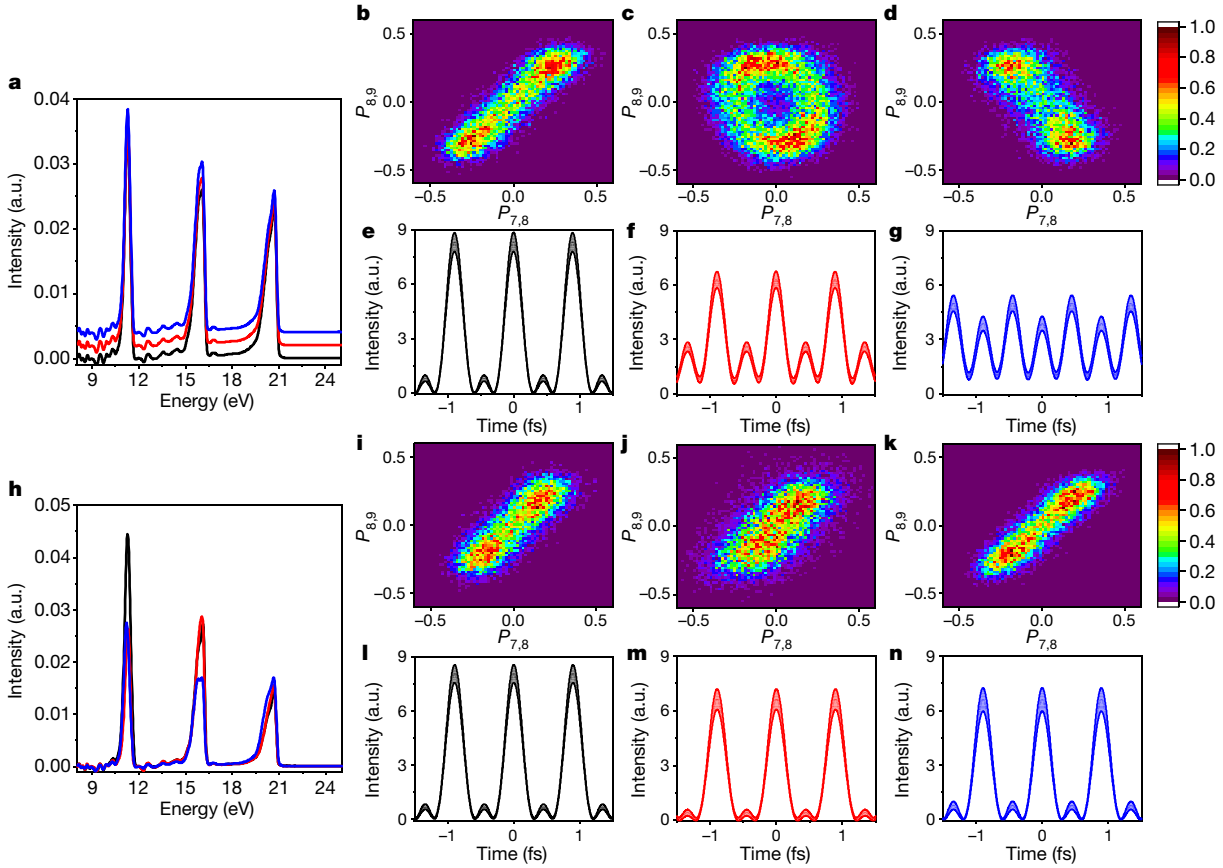

Fig. 3 | Complete phase and amplitude shaping of attosecond waveforms. a–**g**, Photoelectron spectra (**a**), correlation plots of the oscillating components of the sidebands ($P_{7,8}$, $P_{8,9}$; **b**, **c**, **d**) and reconstructed attosecond waveforms (**e**, **f**, **g**) in the case of independent phase shaping for three phase differences $\Delta\varphi_{7,8,9}$ (black curve and panels **b**, **e**; red curve and panels **c**, **f**; blue curve and panels **d**, **g**). The colour scale indicates the density of single-shot experimental points normalized to unity for each panel. The three photoelectron spectra in **a** were vertically shifted for visual clarity. **h**–**n**, Photoelectron spectra (**h**), correlation plots of the oscillating components of the sidebands ($P_{7,8}$, $P_{8,9}$; **i**, **j**, **k**) and reconstructed attosecond waveforms (**l**, **m**, **n**) in the case of independent amplitude control for three settings of the harmonic amplitudes (black curve and panels **i**, **l**; red curve and panels **j**, **m**; blue curve and panels **k**, **n**) using the same values of the phase shifters. The colour scale indicates the density of single-shot experimental points normalized to unity for each panel. See Extended Data Table 3 for additional information on the phase difference $\Delta\varphi_{7,8,9}$ and the amplitude of the harmonics F_7, F_8 and F_9. The errors in the reconstruction of the attosecond pulse trains are determined by the error bars for the amplitudes and phase differences (see Extended Data Table 3) and are indicated as shaded areas in **e**, **f**, **g**, **l**, **m**, **n**.

the possibility of accumulating data over several single-shot measurements, thus improving the signal-to-noise ratio and reducing the error in the temporal reconstruction. In the case of a self-amplified spontaneous emission FEL, pulse properties change on a shot-to-shot basis and a single-shot technique is therefore mandatory[16].

We exploited this approach to the determination of the relative phase of XUV harmonics to demonstrate the independent phase–amplitude shaping capability of attosecond waveforms offered by the FEL FERMI. Figure 3a and Fig. 3b, c and d show three photoelectron spectra and the corresponding correlation plots for three phase differences $\Delta\varphi_{7,8,9}$, respectively. The phase change does not appreciably modify the intensities of the three harmonics (for the amplitudes F_j of the single jth harmonic and for the phase differences see Extended Data Table 3). The reconstructed intensity profiles $I(t)$ are presented in Fig. 3e, f and g. The measurements indicate a pure phase shaping of the harmonic comb: a well-defined attosecond pulse train (Fig. 3e) obtained for $\Delta\varphi_{7,8,9} = 0.08 \pm 0.08$ rad (close to the ideal condition of harmonics in phase, $\Delta\varphi_{7,8,9} = 0$) is transformed first into an attosecond pulse train of lower amplitude with a satellite (Fig. 3f) when $\Delta\varphi_{7,8,9} = 1.93 \pm 0.03$ rad, and finally into an attosecond pulse train characterized by a double structure for $\Delta\varphi_{7,8,9} = 3.29 \pm 0.24$ rad (Fig. 3g), which is close to the condition of harmonics out of phase, $\Delta\varphi_{7,8,9} = \pi$. Figure 3h shows three photoelectron spectra corresponding to three different settings of the amplitudes of the three harmonics (see Extended Data Table 3). The amplitude of the single harmonic was modified by about 25% using the dispersive section and the undulator gaps (see Supplementary Information). Figure 3i, j and k show the correlation plots for the same position of the phase shifters. The phase difference $\Delta\varphi_{7,8,9}$ remains constant within the experimental error, independent of the variations of the single harmonic intensity. The reconstructed attosecond pulse trains for the three configurations are presented in Fig. 3l, m and n. These data demonstrate a pure amplitude shaping of the harmonic comb: the well-defined attosecond pulse structure ($\Delta\varphi_{7,8,9}$ is close to zero (2π) for the three measurements) is preserved for the three configurations and the different harmonic intensities lead only to a variation in the maxima of the intensity profiles. The energy of the attosecond pulse train was about 16 μJ. Table-top-based HHG sources yield much lower energies (in the nanojoule range), and only a few experimental groups have reported total pulse energies on target approaching the microjoule range[23,24].

We estimated that a pulse energy of about 50 nJ per harmonic is sufficient for the acquisition of single-shot photoelectron spectra, which is well below the typical energy per harmonic (a few microjoules) available at FERMI. The currently available range of seed wavelengths at FERMI (360–230 nm) would allow a moderate control of the comb periodicity around 1 fs, but a revised layout of the seed laser optimized for this task

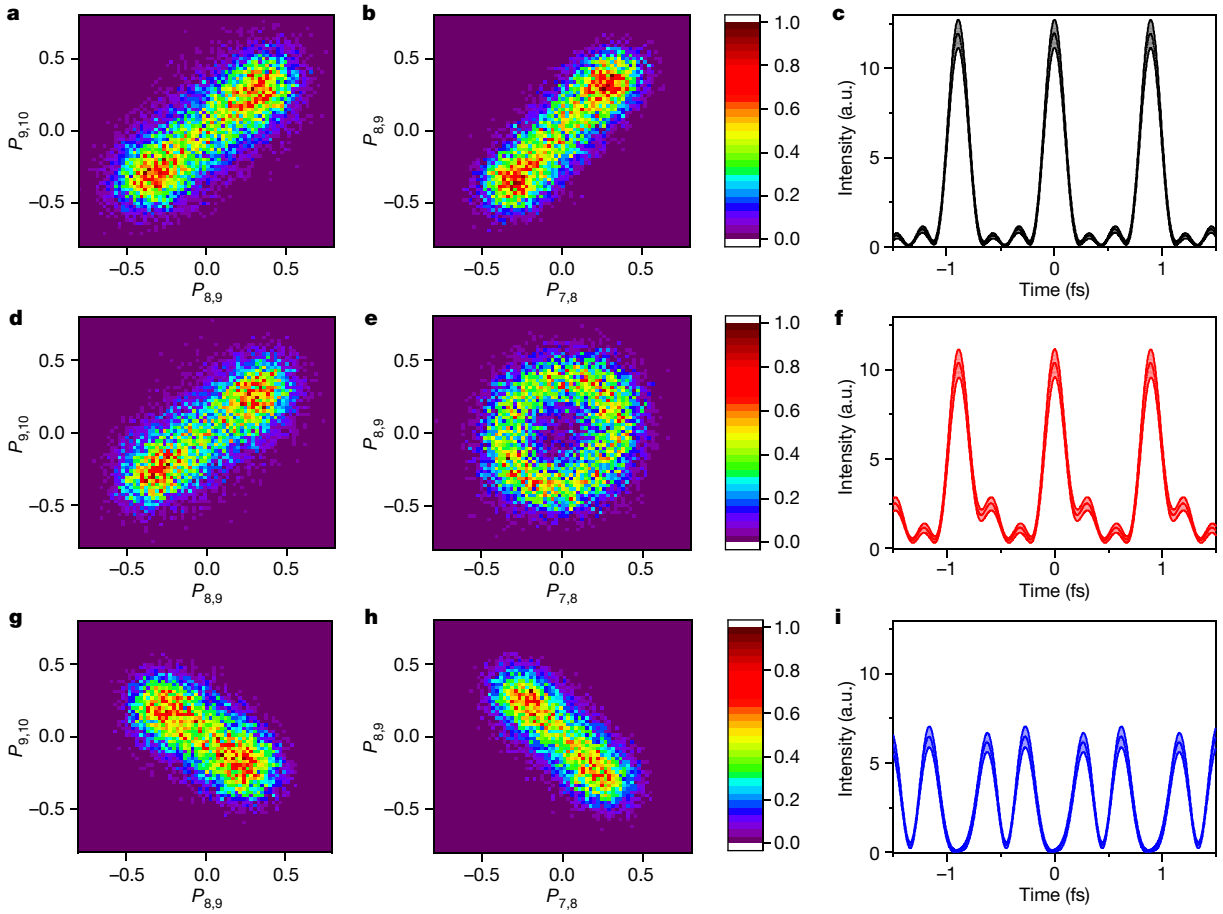

Fig. 4 | Synthesis of complex attosecond waveforms. a–i, Correlation plots of the oscillating components of the sidebands $P_{8,9}$, $P_{9,10}$ (**a**, **d**, **g**) and $P_{7,8}$, $P_{8,9}$ (**b**, **e**, **h**) and retrieved attosecond waveforms (**c**, **f**, **i**) for the four-harmonic experiment and three different combinations of the phase differences $\Delta\varphi_{7,8,9}$ and $\Delta\varphi_{8,9,10}$ (**a**–**c**; **d**–**f**; **g**–**i**). The colour scale indicates the density of single-shot experimental points normalized to unity for each panel. See Extended Data Table 3 for additional information on the phase differences $\Delta\varphi_{7,8,9}$ and $\Delta\varphi_{8,9,10}$, and the amplitude of the harmonics F_7, F_8, F_9 and F_{10}. The errors in the reconstruction of the attosecond pulse trains are determined by the error bars for the amplitudes and phase differences (see Extended Data Table 3) and are indicated as shaded areas in **c**, **f**, **i**.

could increase the spike separation to tens of femtoseconds. Shorter separations can already be achieved by using only odd or only even harmonics (for example, $q = 6, 8, 10$).

We should point out that alternative FEL-based approaches have been theoretically proposed for the generation of a train of attosecond pulses[25,26]. Even though the predicted peak power levels (gigawatts) and pulse durations (down to sub-100 as) are comparable with those reported here, or in principle achievable with our approach, these methods do not offer a strategy for controlling the relative amplitudes and phases of the single harmonics, that is, for attosecond pulse shaping. Extension of our approach to wavelengths as short as 4 nm (300 eV) appear feasible if combined with the echo-enabled harmonic generation seeding scheme[27]. Numerical simulations indicate that the method for the temporal characterization could be applied for photon energies from about 20 eV up to 300 eV, using a suitable gas target.

As a first demonstration of complex attosecond waveform shaping, we considered the case of four harmonics (see Fig. 4), for which the attosecond temporal structure depends on the two phase differences $\Delta\varphi_{7,8,9}$ and $\Delta\varphi_{8,9,10}$. The photoelectron spectra with (red curve) and without (black curve) NIR are shown in Extended Data Fig. 1d. The independent control of the two phases gives the opportunity to generate ultrashort (chirp-free) attosecond pulse trains, as shown in Fig. 4a–c, which report the correlation plots ($P_{8,9}$–$P_{9,10}$ in Fig. 4a and $P_{7,8}$–$P_{8,9}$ in Fig. 4b) in the case of maximum positive correlation (see Extended Data Table 3 for the values of the amplitude and phase differences). The reconstruction (Fig. 4c) returns a duration (FWHM) of the single pulse of about 210 ± 4 as. Figure 4d and e present the results corresponding respectively to $\Delta\varphi_{8,9,10} = 0.20 \pm 0.15$ rad (close to the configuration of harmonics in phase, $\Delta\varphi_{8,9,10} = 0$) and $\Delta\varphi_{7,8,9} = 1.23 \pm 0.06$ rad (harmonics only partially in phase). In the temporal domain, this condition translates into a partial broadening of the peaks (FWHM = 220 ± 5 as) and the appearance of small satellites in the reconstructed attosecond pulse train (Fig. 4f). Finally, Fig. 4g and h present the results when $\Delta\varphi_{8,9,10} = 2.89 \pm 0.08$ rad and $\Delta\varphi_{7,8,9} = 2.95 \pm 0.09$ rad (that is, both phase differences are close to π), respectively: the four harmonics are divided into two groups (harmonics 7 and 8, and harmonics 9 and 10), each pair of which is (approximately) in phase, with an additional phase jump of π between the two groups. This condition leads to a double attosecond pulse structure, which is visible in the reconstruction presented in Fig. 4i. The availability of six undulators at FERMI would in principle allow for the generation of six harmonics. This configuration may, however, require a revised and optimized setup. Simulations indicate that the experimental technique demonstrated in this work could be extended to the characterization of pulses with durations in the sub-100-as regime.

Our technique also offers the possibility of determining with subcycle resolution the relative phase of the XUV and NIR pulses, enabling phase-resolved pump–probe experiments at FELs based on attosecond pulse trains (see Supplementary Information and Extended Data Fig. 4). The high intensities in the XUV and X-ray spectral region reached by FELs,

combined with the capabilities offered by seeding to independently control and shape the amplitudes and phases of attosecond pulses, will open new possibilities for the investigation and control of ultrafast nonlinear electronic processes. The design of future seeded FEL sources at other facilities such as LCLS[28], FLASH[29] and SINAP[30] could be modified to optimize them for the mode of operation described here, which is at present possible at FERMI[17] and DALIAN[31]. In solid samples, attosecond shaped waveforms could be used to promote electrons from the inner-valence to the conduction band, giving the possibility of investigating diffusion and relaxation effects with attosecond resolution and with temporally sculpted electronic wave packets. More generally, our results give unprecedented access to programmable attosecond waveforms at high intensities.

Online content

Any methods, additional references, Nature Research reporting summaries, source data, extended data, supplementary information, acknowledgements, peer review information; details of author contributions and competing interests; and statements of data and code availability are available at https://doi.org/10.1038/s41586-020-2005-6.

1. Krausz, F. & Ivanov, M. Attosecond physics. *Rev. Mod. Phys.* **81**, 163–234 (2009).
2. Corkum, P. B. & Krausz, F. Attosecond science. *Nat. Phys.* **3**, 381–387 (2007).
3. Kapteyn, H., Cohen, O., Christov, I. & Murnane, M. Harnessing attosecond science in the quest for coherent X-rays. *Science* **317**, 775–778 (2007).
4. Paul, P. M. et al. Observation of a train of attosecond pulses from high harmonic generation. *Science* **292**, 1689–1692 (2001).
5. Kienberger, R. et al. Atomic transient recorder. *Nature* **427**, 817–821 (2004).
6. Tzallas, P., Charalambidis, D., Papadogiannis, N. A., Witte, K. & Tsakiris, G. D. Direct observation of attosecond light bunching. *Nature* **426**, 267–271 (2003).
7. Nabekawa, Y. et al. Interferometric autocorrelation of an attosecond pulse train in the single-cycle regime. *Phys. Rev. Lett.* **97**, 153904 (2006).
8. López-Martens, R. et al. Amplitude and phase control of attosecond light pulses. *Phys. Rev. Lett.* **94**, 033001 (2005).
9. Gustafsson, E. et al. Broadband attosecond pulse shaping. *Opt. Lett.* **32**, 1353–1355 (2007).
10. Hofstetter, M. et al. Attosecond dispersion control by extreme ultraviolet multilayer mirrors. *Opt. Express* **19**, 1767–1776 (2011).
11. Bartels, R. et al. Shaped-pulse optimization of coherent emission of high-harmonic soft X-rays. *Nature* **406**, 164–166 (2000).
12. Ackermann, W. et al. Operation of a free-electron laser from the extreme ultraviolet to the water window. *Nat. Photon.* **1**, 336–342 (2007).
13. Emma, P. et al. First lasing and operation of an ängstrom-wavelength free-electron laser. *Nat. Photon.* **4**, 641–647 (2010).
14. Marinelli, A. et al. Experimental demonstration of a single-spike hard-X-ray free electron-laser starting from noise. *Appl. Phys. Lett.* **111**, 151101 (2017).
15. Huang, S. et al. Generating single-spike hard X-ray pulses with nonlinear bunch compression in free-electron lasers. *Phys. Rev. Lett.* **119**, 154801 (2017).
16. Hartmann, N. et al. Attosecond time–energy structure of X-ray free-electron laser pulses. *Nat. Photon.* **12**, 215–220 (2018).
17. Allaria, E. et al. Highly coherent and stable pulses from the FERMI seeded free-electron laser in the extreme ultraviolet. *Nat. Photon.* **6**, 699–704 (2012).
18. Mairesse, Y. et al. Attosecond synchronization of high-harmonic soft X-rays. *Science* **302**, 1540–1543 (2003).
19. Schulz, S. et al. Femtosecond all-optical synchronisation of an X-ray free-electron laser. *Nat. Commun.* **6**, 5938 (2015).
20. Danailov, M. B. et al. Towards jitter-free pump-probe measurements at seeded free electron laser facilities. *Opt. Express* **22**, 12869–12879 (2014).
21. Prince, K. C. et al. Coherent control with a short-wavelength free-electron laser. *Nat. Photon.* **10**, 176–179 (2016).
22. Iablonskyi, D. et al. Observation and control of laser-enabled Auger decay. *Phys. Rev. Lett.* **119**, 073203 (2017).
23. Takahashi, E. J. et al. Attosecond nonlinear optics using gigawatt-scale isolated attosecond pulses. *Nat. Commun.* **4**, 2691 (2013).
24. Nayak, A. et al. Multiple ionization of argon via multi-XUV-photon absorption induced by 20-GW high-order harmonic laser pulses. *Phys. Rev. A* **98**, 023426 (2018).
25. Zholents, A. A. Method of an enhanced self-amplified spontaneous emission for x-ray free electron lasers. *Phys. Rev. Spec. Top. Accel. Beams* **8**, 040701 (2005).
26. Thompson, N. R. & McNeil, B. W. J. Mode locking in a free-electron laser amplifier. *Phys. Rev. Lett.* **100**, 203901 (2008).
27. Ribič, P. R. et al. Coherent soft X-ray pulses from an echo-enabled harmonic generation free-electron laser. *Nat. Photon.* **13**, 555–561 (2019).
28. Hemsing, E. et al. *Soft X-ray FEL Seeding Studies for LCLS-II: Task Force Status Report. A White Paper by SLAC and LBNL*. Technical Note SLAC-TN-19-001 (SLAC, 2019); available at https://www.slac.stanford.edu/pubs/slactns/tn06/slac-tn-19-001.pdf (2019).
29. Grattoni, V. et al. Status of seeding development at sFLASH. In *Proc. FEL2017* (eds Bishofberger, K., Carlsten, B. & Schaa, V. R. W.) 136–139 (JACoW, 2018).
30. Zhao, Z. et al. Status of the SXFEL facility. *Appl. Sci.* **7**, 607 (2017).
31. Yong, Y. et al. Dalian extreme ultraviolet coherent light source. *Chin. J. Lasers* **46**, 0100005 (2019).

Methods

Experimental setup

The experiment was performed at the seeded FEL FERMI and is schematically presented in Extended Data Fig. 1. Two different configurations of the undulators were implemented for the generation of three (Extended Data Fig. 1a) and four (Extended Data Fig. 1b) harmonics. The parameters of the FEL harmonics are reported in Extended Data Table 1. The seeding parameters (seed laser power and strength of the dispersive section) were carefully optimized in order to produce a sufficiently high bunching that could be preserved along the whole set of undulators tuned at the various harmonics. Tuning the first undulators to higher harmonics (shorter wavelengths) and the later ones to the lower harmonics had a twofold motivation. First, the bunching at higher harmonics was more prone to degradation and it would have been more difficult to preserve it up to the end of the undulator chain. Second, the diffraction at longer wavelengths was larger thus a shorter propagation path was preferable. For a properly optimized setup each undulator group produced a coherent, ~50-fs-long FEL pulse centred at the resonant wavelength[32]. The phase between the electric field of each harmonic was determined and controlled by the phase shifter available at FERMI at each undulator break.

The XUV and NIR pulses (energy $E_{NIR} = 45$ μJ, duration $FWHM_{NIR} = 60$ fs, intensity $I_{NIR} = 1.5 \times 10^{12}$ W cm^{-2}) were temporally and spatially overlapped in the interaction region with a residual shot-to-shot delay jitter of $\Delta\tau = \pm 3$ fs using a recombination mirror for collinear propagation. The single-shot photoelectron spectra, with (red lines) and without (black lines) the NIR pulse for the three and four harmonics configurations (see Extended Data Fig. 1c, d, respectively), were measured in neon using a magnetic bottle electron spectrometer placed in the interaction region (see Extended Data Fig. 1e). Only photoelectrons emitted in the upward hemisphere were collected, as shown by the detection efficiency (see Extended Data Fig. 1f) as a function of the angle between the emission direction and the spectrometer axis (which coincides with the (vertical) direction of polarization of the FEL pulses (see Supplementary Information)). For each machine setting, single-shot harmonic spectra (without NIR field) were measured[33]. From these data we estimated a typical shot-to-shot fluctuation (standard deviation) for the intensity of each harmonic of about 5%–8%. The energy of the single harmonic was proportional to the integral of the corresponding peak of the photoelectron spectrum. The integral was corrected for the response function of the magnetic bottle spectrometer for different photoelectron energies, the cross-section of the target gas, and the transmission of the XUV beamline[17].

The data were accumulated typically for about 10,000–12,000 shots for each machine and phase setting. For each setting, the mean intensities of the main photoelectron peaks I_q ($q = (7, 8, 9)$ or $q = (7, 8, 9, 10)$) were determined.

The total energy of the FEL pulse was measured (on a single-shot basis) with an ionization monitor placed upstream of the transmission and focusing XUV beamline.

Reconstruction of attosecond pulses

The temporal reconstruction of the attosecond pulse train using the correlation parameter $\rho_{q-1,q,q+1}$ for the simulations presented in Fig. 1c–f is shown in Extended Data Fig. 5a–d, respectively. The agreement between the input data (black curves) and the reconstructed profiles (red (Extended Data Fig. 5a), blue (Extended Data Fig. 5b), green (Extended Data Fig. 5c), and magenta (Extended Data Fig. 5d)) indicates the validity of our reconstruction method based on the value of the correlation parameter $\rho_{7,8,9}$. We also performed time-dependent Schrödinger equation (TDSE) simulations which confirmed the validity of our reconstruction protocol. The correlation curve obtained using the TDSE simulations reproduces that obtained by the strong field approximation (SFA) with a small shift of 0.157 rad, which results in only minor corrections in the reconstruction of the intensity profile of the attosecond pulses. This shift was taken into account in the reconstructions presented in the manuscript.

The validity of the temporal reconstruction of the attosecond pulse train from the shift of the oscillations of the sidebands $S^{(+)}_{q-1,q}$ $\left(S^{(-)}_{q-1,q}\right)$ and $S^{(+)}_{q,q+1}$ $\left(S^{(-)}_{q,q+1}\right)$ is shown in Extended Data Fig. 5e, which reports the input (black lines) and reconstructed (blue dotted lines) intensity profiles for the simulation shown in Fig. 1b.

Simulations for attosecond pulse generation

The emission process for the configuration emitting harmonics 7, 8 and 9 can be simulated with the new version of the FEL code GENESIS 1.3[34]. With the undulator set in the condition reported in Extended Data Fig. 1a, the resonant wavelength to be followed by the FEL code is different in the three sets of undulators. Given the fact that GENESIS 1.3 only tracks a relatively narrow band field this requires that different simulations are performed for the different sets of undulators. This option is normally used for harmonic generation FEL schemes and has been largely used in the study of the high-gain harmonic-generation operation mode implemented at FERMI. The problem is here complicated by the fact that consecutive undulators are tuned to wavelengths that are not integer multiples of one another. The recent upgrade of GENESIS 1.3 allows tracking of each single electron in the beam. The simulation can be performed if one carefully manages the transition from one undulator set to the next. After the interaction with the external seed laser is simulated, and the energy modulation at the 260 nm wavelength is imprinted in the beam, the particle phase-space is used to simulate the emission process at the ninth harmonic in the first group of undulators. The electric field produced here is then propagated in free space to the exit of the whole radiator, while the electrons are used for simulating the emission process at the eighth harmonic in the second group of undulators. The same is done with fields and electrons entering the third group of undulators. Finally, three fields are produced representing the emission from each undulator set at the exit of the radiator. The result of the simulation is presented in Extended Data Fig. 6a, b that shows the femtosecond envelope (Extended Data Fig. 6a) and the attosecond structure (Extended Data Fig. 6b) of the XUV pulse obtained using the combination of the three harmonics. The resonance condition, phase shifts between sets of undulators, and other parameters can be adjusted as usual. Simulations rely on the standard electron beam and seed laser for FERMI. Seed laser power and strength of the dispersive section are used as an optimization parameter to maximize the bunching and keep emission balanced between various harmonics. The parameters used in the simulation are summarized in Extended Data Table 4.

Data availability

Raw data were generated at the FERMI large-scale facility. Derived data supporting the findings of this study are available from the corresponding author on reasonable request.

32. Finetti, P. et al. Pulse duration of seeded free-electron lasers. *Phys. Rev. X* **7**, 021043 (2017).
33. Zangrando, M. et al. Recent results of PADReS, the Photon Analysis Delivery and REduction System, from the FERMI FEL commissioning and user operations. *J. Synchr. Rad.* **22**, 565–570 (2015).
34. Reiche, S. Update on the FEL code GENESIS 1.3. In *Proc. 36th Int. Free Electron Laser Conf. (FEL'14)* (eds Chrin, J., Reiche, S. & Schaa, V. R. W.) TUP019, 403–407 (JACoW, 2014).

Acknowledgements This project received funding from the European Union's Horizon 2020 research and innovation programme under the Marie Sklodowska-Curie grant agreement no. 641789 MEDEA and the Italian Ministry of Research (Project FIRB no. RBID08CRXK). K.U. acknowledges support from the X-ray Free Electron Laser Utilization Research Project and the X-ray Free Electron Laser Priority Strategy Program of the Ministry of Education, Culture, Sports, Science and Technology of Japan (MEXT), from the Cooperative Research Program 'Network Joint Research Center for Materials and Devices: Dynamic Alliance for Open Innovation Bridging Human, Environment and Materials', from the bilateral project CNR-JSPS

'Ultrafast science with extreme ultraviolet Free Electron Lasers', and from the IMRAM project for international co-operation. R.F. and J.M. thank the Swedish Research Council (VR) and the Knut and Alice Wallenberg Foundation for financial support. E.V.G. acknowledges support from the Foundation for the Advancement of Theoretical Physics and Mathematics 'BASIS'. M. Meyer and T.M. acknowledge support from the Deutsche Forschungsgemeinschaft (DFG) under grant no. SFB925/1. A.A.L. was supported by the US Department of Energy contract no. DE-AC02-76SF00515. Research at Louisiana State University was supported by the US Department of Energy, Office of Science, Basic Energy Sciences, under contract no. de-sc0010431. Portions of this research were conducted with high performance computing resources provided by Louisiana State University (http://www.hpc.lsu.edu) and by Louisiana Optical Network Infrastructure (http://hpc.loni.org). G.S. acknowledges useful discussions about the simulations and the data analysis with T. Pfeifer and M. Kübel. We acknowledge L. Foglia, A. Simoncig and M. Coreno for valuable discussions.

Author contributions P.K.M., M. Moioli, D.E., M.D.F., O.P., H.A., P.C., T.M., M. Meyer, S.B., N.I., E.R.S., J.M., T.C., M.D., S.K., H.N.G., D.Y., K.U., K.C.P., C.G. and C.C. contributed to data acquisition and to data analysis. L.G., E.A., G.D.N., C.S., G.P. and S.S. operated the machine and designed the three and four harmonic generation scheme. A.A.L. contributed to the machine operation. A.D. and M. B. D. designed the beam path for the NIR pulse. P.F. designed the mechanics for the recombination mirror. A.D. and C.G. designed the recombination mirror, and the whole set-up was installed by A.D., C.G. and M.D.F. A.D. and M.D.F. designed and installed the beam dump diagnostic system for alignment of the collinear configuration. M.D.F., O.P. and C.C. prepared the end station. R.B., G.K., C.E.S.D.R. and F.B. developed the analysis tools used during beamtime. M.R. contributed to the preliminary development of the simulation codes. M.L., J.E.B. and K.J.S. performed the TDSE calculations. R.J.S. and R.F. constructed and operated the magnetic bottle electron spectrometer. A.N.G.-G. and E.V.G. developed the perturbation-theory approach and derived the atomic phase contributions. C.C. and G.S. conceived the idea of the experiment. G.S. developed the numerical code for the SFA simulations. P.K.M. developed the numerical code for the correlation analysis. P.K.M., C.C. and G.S. analysed the experimental data and performed the simulations. G.S. supervised the work. P.K.M., A.N.G.-G., E.V.G., C.C. and G.S. wrote the manuscript, which was discussed and agreed by all coauthors.

Competing interests The authors declare no competing interests.

Additional information

Supplementary information is available for this paper at https://doi.org/10.1038/s41586-020-2005-6.

Correspondence and requests for materials should be addressed to G.S.

Peer review information *Nature* thanks Eduard Prat Costa, Makina Yabashi and the other, anonymous, reviewer(s) for their contribution to the peer review of this work.

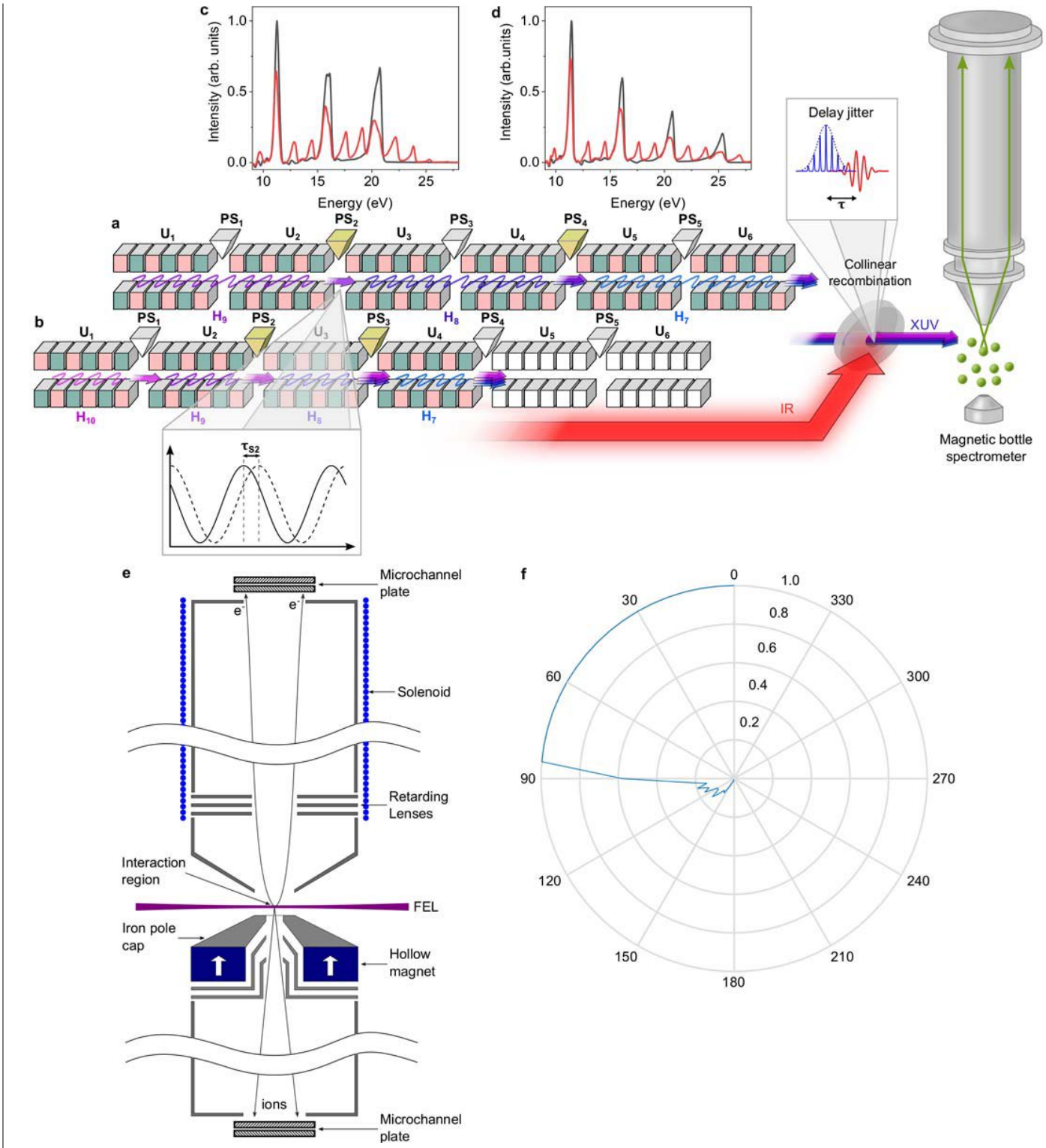

Extended Data Fig. 1 | Free-electron laser configuration for the generation of multiple harmonics and experimental setup. a, **b**, Configurations of the six undulators (U_1–U_6) for the generation of three (**a**) and four (**b**) harmonics. In the first case, two undulators per harmonic were used, while in the second case, each harmonic was generated by one undulator only. The phase-shifters (PS_1–PS_5) used to control the relative phase between the harmonics are indicated in yellow for the two configurations. **c**, **d**, Typical single-shot photoelectron spectra without (black lines) and with (red lines) the NIR pulse, measured for the three (**c**) and four (**d**) harmonic cases. **e**, Schematic, half-section view of the spectrometer, including the ion flight tube (bottom) and electron flight tube (top). **f**, Normalized simulated geometrical collection efficiency as a function of polar emission angle for 2–42 eV electrons, using a cylindrical magnet configuration with the pole placed 5 mm away from the interaction region. Electrons were simulated using steps of 5 eV. An emission angle of 0° (180°) corresponds to the axis of the spectrometer in (away from) the direction of the electron detector.

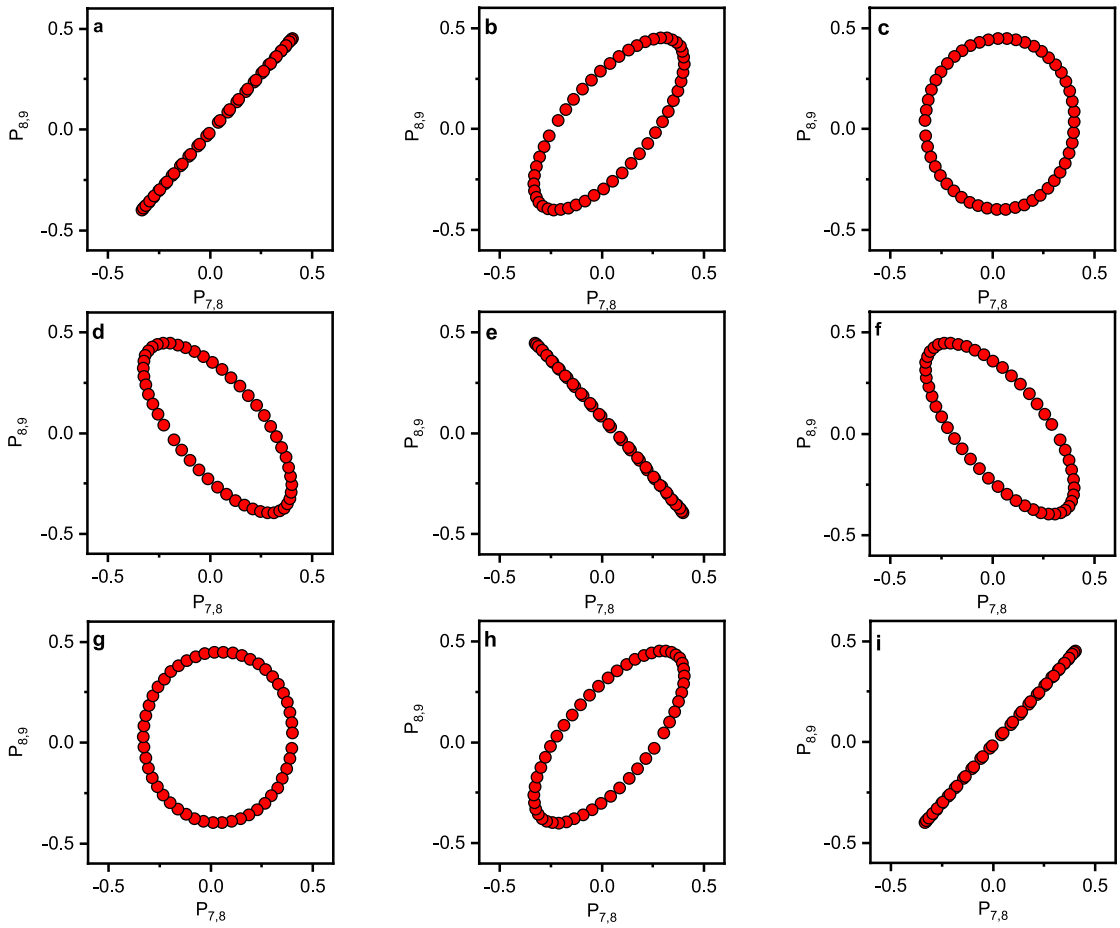

Extended Data Fig. 2 | Simulated correlation plots. Shown are simulated correlation plots ($P_{8,9}$, $P_{7,8}$) for different values of $\Delta\varphi_{7,8,9}$ from 0 to 2π in steps of π/4: $\Delta\varphi_{7,8,9}$ = 0 (**a**), π/4 (**b**), π/2 (**c**), 3π/4 (**d**), π (**e**), 5π/4 (**f**), 3π/2 (**g**), 7π/4 (**h**) and 2π (**i**). The intensities of the three harmonics are equal.

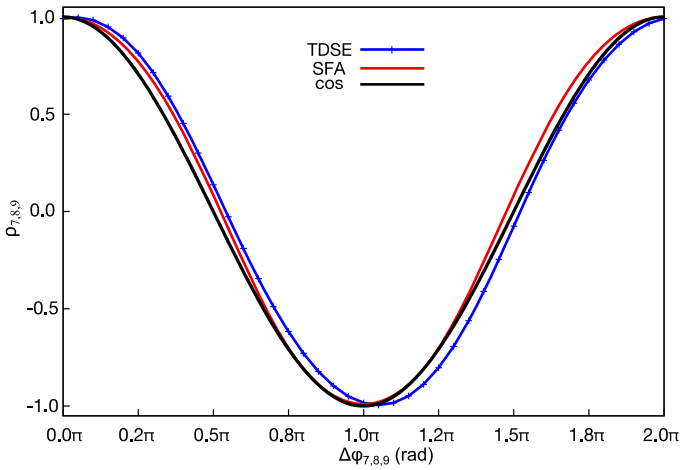

Extended Data Fig. 3 | Simulated correlation parameter $\rho_{7,8,9}$. Evolution of the correlation parameter $\rho_{7,8,9}$ as a function of the phase difference $\Delta\varphi_{7,8,9}$ simulated using the SFA (red) and the TDSE (blue). The black curve indicates a cosine evolution.

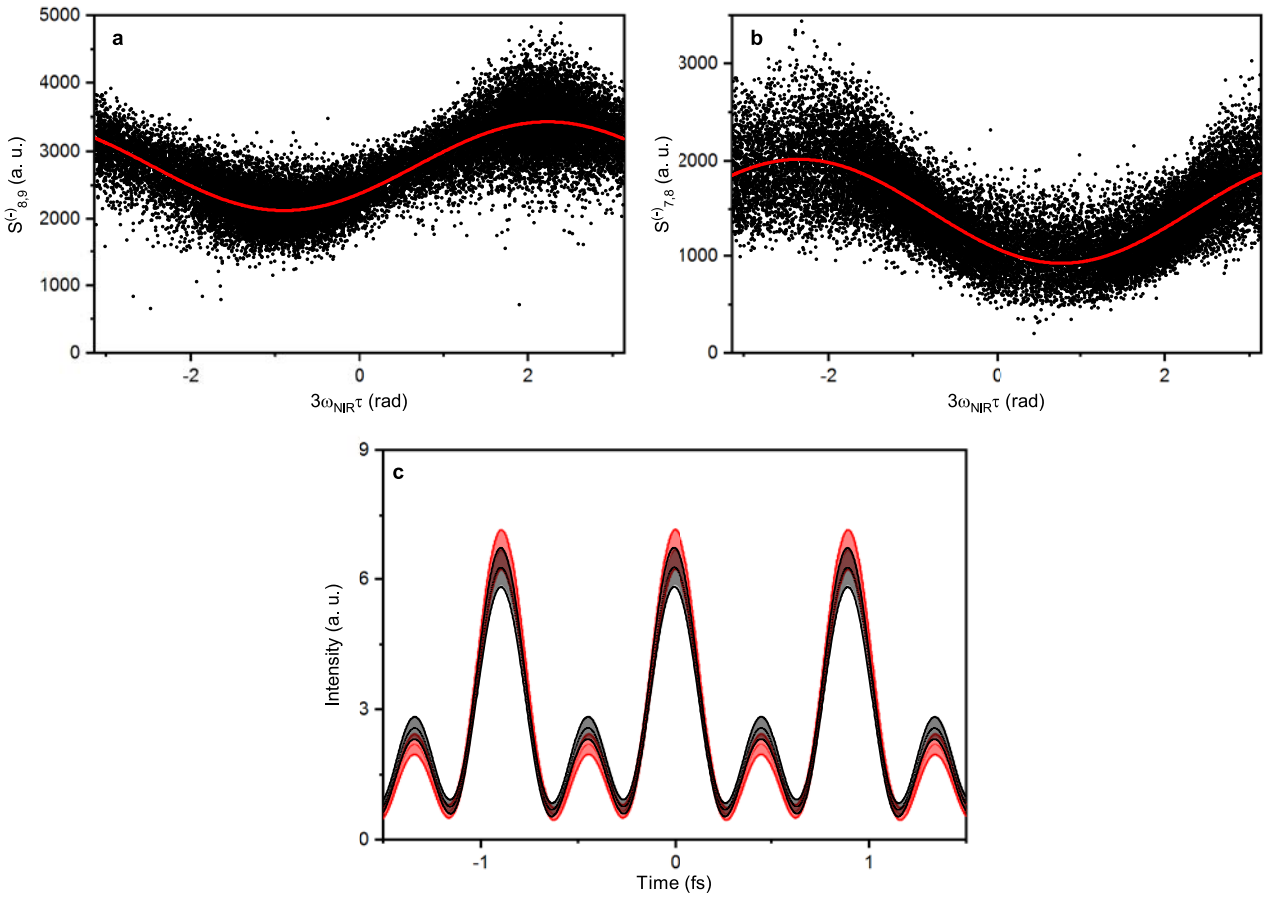

Extended Data Fig. 4 | Phase reordering of single-shot sideband intensities. **a**, **b**, Intensity of the sidebands $S^{(-)}_{8,9}$ (**a**) and $S^{(-)}_{7,8}$ (**b**) (black points) as a function of the relative phase $3\omega_{NIR}\tau$ between the attosecond pulse train and the NIR field. The red curves show sinusoidal fits of the distributions. **c**, Comparison of the reconstructed attosecond pulse train using the correlation parameter method $\rho_{7,8,9}$ (black curve) and the 'reconstruction of attosecond beating by interference of two-photon transitions' method (red curve) based on the phase differences extracted from the sinusoidal fits. The second method is typically used for the characterization of attosecond pulse trains produced by HHG. The error in the reconstructions is indicated by the shaded areas.

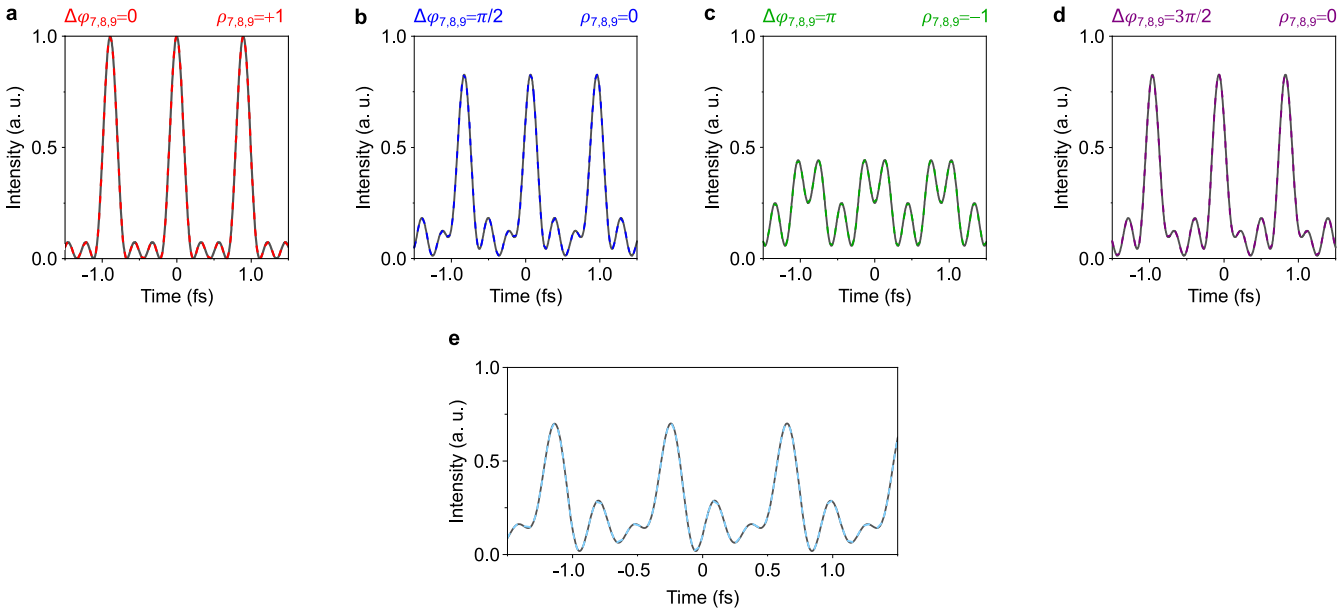

Extended Data Fig. 5 | Reconstruction of attosecond pulses for multi-NIR photon transitions. a–**d**, Input (black line) and reconstructed (**a**, red line; **b**, blue line; **c**, green line; and **d**, magenta line) intensity profiles of the attosecond train, corresponding to Fig. 1c–f for phase differences $\Delta\varphi_{7,8,9} = 0$ (**a**), π/2 (**b**), π (**c**) and 3π/2 (**d**). **e**, Reconstruction of attosecond pulses from sideband oscillations for multi-NIR photon transitions for the trace presented in Fig. 1b (input (black line) and reconstructed (blue dotted line) intensity profiles). The intensity of the NIR pulse is $I_{NIR} = 1.5 \times 10^{11}$ W cm^{-2}. The relative phases between the harmonics are: $\varphi_{10} - \varphi_9 = 108°$, $\varphi_9 - \varphi_8 = 160°$ and $\varphi_8 - \varphi_7 = 8°$.

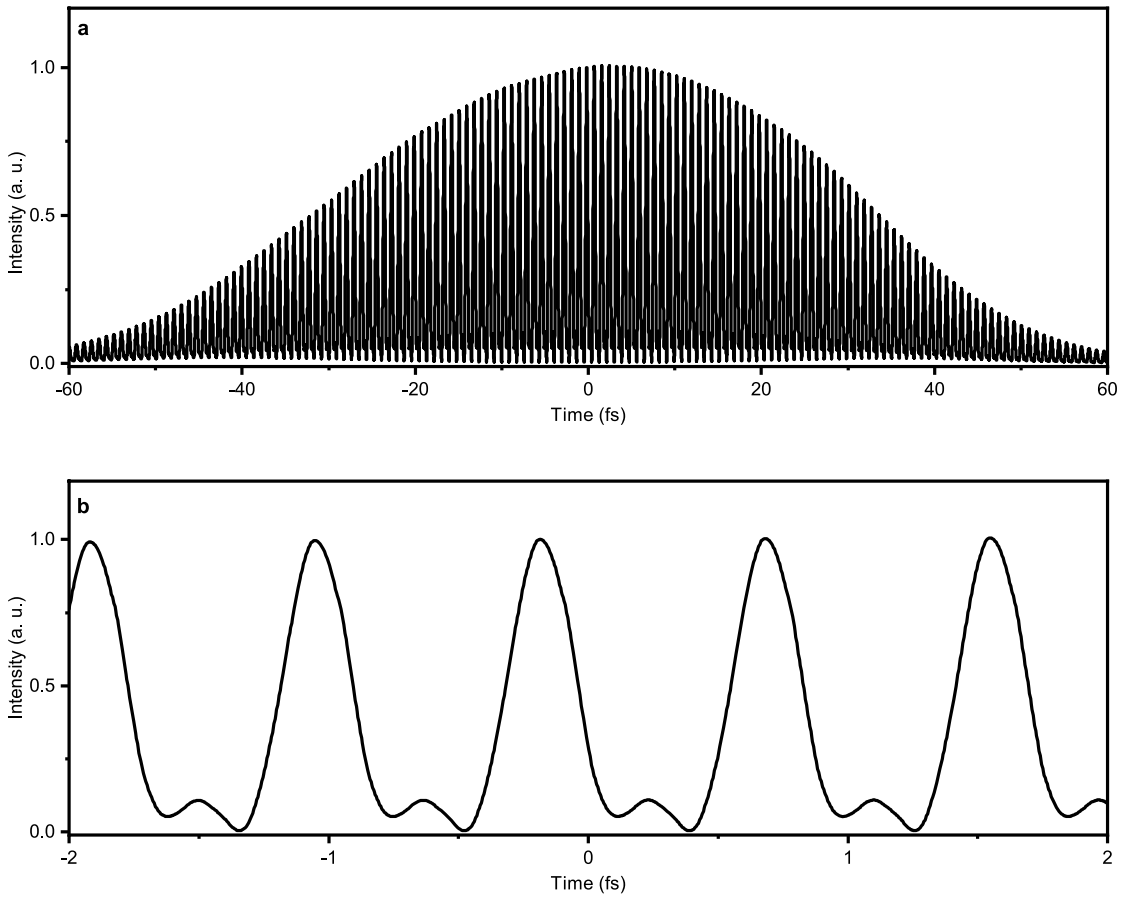

Extended Data Fig. 6 | GENESIS 1.3 simulations. Shown is the attosecond pulse train simulated using the GENESIS 1.3 code: **a**, complete temporal evolution of the train, and **b**, magnified view of the attosecond pulses in the train.

Extended Data Table 1 | XUV experimental parameters

	Harmonic	Photon energy (eV)	Energy (μJ)	Duration (fs)	Intensity (W/cm^2)
Three harmonics	7	32.88 ± 0.03	4.21 ± 0.58	50 ± 5	(1.1 ± 0.2) x 10^{14}
	8	37.57 ± 0.04	5.29 ± 0.58	50 ± 5	(1.5 ± 0.2) x 10^{14}
	9	42.27 ± 0.04	6.7 ± 1.2	50 ± 5	(1.9 ± 0.4) x 10^{14}
Four harmonics	7	32.88 ± 0.03	1.01 ± 0.12	50 ± 5	(2.8 ± 0.4) x 10^{13}
	8	37.57 ± 0.04	0.95 ± 0.12	50 ± 5	(2.6 ± 0.4) x 10^{13}
	9	42.27 ± 0.04	0.67 ± 0.11	50 ± 5	(1.9 ± 0.4) x 10^{13}
	10	46.96 ± 0.05	0.40 ± 0.50	50 ± 5	(1.1 ± 0.3) x 10^{13}

Measured harmonic order, photon energy, energy of the single harmonic and intensity of the single harmonic for the three- and four-harmonic experiments. For the duration of the single harmonic, we used the values reported in ref. [32].

Extended Data Table 2 | Experimental correlation coefficients

Panel	a	b	c	d	e
$\rho_{7,8,9}$	0.83 ± 0.02	0.74 ± 0.01	0.32 ± 0.03	-0.20 ± 0.02	-0.62 ± 0.03
$\Delta\varphi_{7,8,9}$ (rad)	-0.21 ± 0.12	0.50 ± 0.05	1.21 ± 0.05	1.91 ± 0.03	2.62 ± 0.05
Panel	f	g	h	i	j
$\rho_{7,8,9}$	-0.75 ± 0.02	-0.46 ± 0.01	0.14 ± 0.03	0.67 ± 0.01	0.86 ± 0.01
$\Delta\varphi_{7,8,9}$ (rad)	3.33 ± 0.20	4.04 ± 0.03	4.74 ± 0.03	5.45 ± 0.02	6.16 ± 0.02

Correlation coefficients $\rho_{7,8,9}$ and phase differences $\Delta\varphi_{7,8,9}$ for the measurements presented in the panels of Fig. 2 in the main text.

Extended Data Table 3 | Amplitudes and harmonic phase differences

	Figure	F_{10}	F_9	F_8	F_7	$\Delta\varphi_{8,9,10}$ (rad)	$\Delta\varphi_{7,8,9}$ (rad)
Three harmonics	3b,e	-	0.95 ± 0.06	1.00 ± 0.03	0.89 ± 0.06	-	0.08 ± 0.08
	3c,f	-	0.94 ± 0.07	1.00 ± 0.03	0.87 ± 0.06	-	1.93 ± 0.03
	3d,g	-	0.92 ± 0.07	1.00 ± 0.03	0.88 ± 0.06	-	3.29 ± 0.24
	3i,l	-	0.75 ± 0.06	1.00 ± 0.04	1.06 ± 0.06	-	6.08 ± 0.07
	3j,m	-	0.78 ± 0.08	1.02 ± 0.04	0.80 ± 0.06	-	6.09 ± 0.40
	3k,n	-	0.85 ± 0.09	0.83 ± 0.05	0.82 ± 0.07	-	6.18 ± 0.12
Four harmonics	4a-c	0.59 ± 0.07	0.76 ± 0.06	1.00 ± 0.05	1.03 ± 0.05	0.20 ± 0.15	5.94 ± 0.04
	4d-f	0.58 ± 0.07	0.77 ± 0.07	1.04 ± 0.05	1.07 ± 0.05	0.20 ± 0.15	1.23 ± 0.06
	4g-i	0.57 ± 0.08	0.77 ± 0.08	1.03 ± 0.06	0.99 ± 0.05	2.89 ± 0.08	2.95 ± 0.09

Amplitudes F_{10}, F_9, F_8 and F_7 and phase differences $\Delta\varphi_{8,9,10}$ and $\Delta\varphi_{7,8,9}$ for the three- (Fig. 3) and four-harmonic cases (Fig. 4). For the phase (amplitude) shaping in the three-harmonic case, the photoelectron spectra were rescaled to the area of the peak corresponding to the eighth harmonic in Fig. 3b and e (Fig. 3i and l). For the four-harmonic case, the photoelectron spectra were rescaled to the area of the eighth harmonic in Fig. 4a–c. For the pulse reconstruction, the measured $\Delta\varphi_{7,8,9}$ phases were corrected for the shift of 0.157 rad obtained by the TDSE simulations.

Extended Data Table 4 | Parameters for the GENESIS 1.3 simulations

Undulator parameters	
U_1-U_2 resonant wavelength	28.889 nm
U_3-U_4 resonant wavelength	32.500 nm
U_5-U_6 resonant wavelength	37.143 nm
Undulator polarisation	linear
PS_1-PS_2	0 rad
Dispersion	60 μm
Seed laser parameters	
Wavelength	260 nm
Power	40 MW
Pulse length (FWHM)	110 fs
Electron beam parameters	
Energy	1.2 GeV
Energy spread	110 keV
Normalized emittance	1 mm rad
Peak current	700 A
Beam size	50 - 70 μm

Parameters used in the GENESIS 1.3 code for simulating the generation of the train of attosecond pulses.